Physical Insights into Chemistry, Catalysis, and Interfaces

Helix Shape Power-Dependent Properties of Single Upconversion Nanoparticles

Jiayan Liao, Dayong Jin, Chaohao Chen, Yiming Li, and Jiajia Zhou

J. Phys. Chem. Lett., **Just Accepted Manuscript** • DOI: 10.1021/acs.jpclett.9b03838 • Publication Date (Web): 24 Jan 2020

Helix shape power-dependent properties of single upconversion nanoparticles

Jiayan Liao[1], Dayong Jin[1,2], Chaohao Chen[1], Yiming Li[3], Jiajia Zhou[1,*]

[1]*Institute for Biomedical Materials &Devices (IBMD), Faculty of Science, University of Technology Sydney, Ultimo, New South Wales, Australia*

[2]*UTS-SUStech Joint Research Centre for Biomedical Materials & Devices, Department of Biomedical Engineering, Southern University of Science and Technology, Shenzhen, Guangdong, P.R.China*

[3]*Department of Biomedical Engineering, Southern University of Science and Technology, Shenzhen, 518055, China.*

** E-mail: jiajia.zhou@uts.edu.au*

Non-blinking, non-bleaching and super-bright single upconversion nanoparticles have been recently discovered with non-linear power-dependent properties and can be switchable under dual beam excitations, which are ideal for super-resolution microscopy, single-molecule tracking, and digital assays. Here, we report that the brightness of Nd^{3+}-Yb^{3+}-Er^{3+} doped nanoparticles displays a pair of unusual double helix shapes as the function of power densities of 976 nm and 808 nm excitations. We systemically analyse the power-dependent emission spectra, lifetimes, and power-intensity double-log slopes of single upconversion nanoparticles, which reveal that the dynamic roles of Nd^{3+} ions in the tri-doped nanosystem with underlining electron population pathways are power dependent. That is, at high power 808 nm excitation, Nd^{3+} ions can directly emit upconverted luminescence, with their conventional role of sensitization saturated in the $Nd^{3}\rightarrow Yb^{3+}\rightarrow Er^{3+}$ energy transfer systems. Moreover, we confirm that the universal helix shape phenomena commonly exist in a set of eight batches of core-shell nanoparticles regardless of the doping concentrations of Nd^{3+}, Yb^{3+} and Er^{3+} ions in the sensitization shell, migration shell, and active core, though the crossing nodes occur at different excitation power ranges. This study emphasizes the important role of power-dependent properties in both improving the upconversion emission efficiency and the design of non-linear responsive probes for imaging and sensing.

Trivalent lanthanide ion (Ln^{3+})-doped upconversion nanoparticles (UCNPs) can convert multiple near-infrared (NIR) photons into shorter wavelength ultraviolet (UV), visible (vis) or NIR luminescence by utilizing real long-lived, ladder-like energy levels of Ln^{3+} ions. The anti-Stokes emissions are immune to the auto-fluorescence background interference, ideally suitable for imaging[1–7] and sensing application[8–13]. UCNPs are made of rigid crystal hosts and can be doped by multiple Ln^{3+} ions, allowing excellent photostability and a great deal of tunability in emission colours, lifetimes and brightness, all highly dependent on the excitation power density following the sophisticated non-linear process.[14–19] Single nanoparticle characterization has played an important role in the discoveries of the many unique properties of UCNPs, including their photo stability, power-dependent doping concentration leading to their super brightness, optical uniformity and switchability under dual wavelength excitations, which lead to a range of recent advances being developed using single UCNPs for applications, such as super-resolution imaging[20,21], single-molecule tracking[22], and digital assay[23–25].

β-$NaYF_4$ UCNPs using Yb^{3+} ions as sensitizers have been broadly explored with laser excitation at 980 nm that overlaps the absorption band of water molecules[26,27]. To avoid the heating damage to biological samples, 915 nm excitation of Yb^{3+} doped α-$NaYF_4$[28], 1532 nm excitation of Er^{3+} doped β-$NaYF_4$ UCNPs[29] and 800 nm excitation of Nd^{3+}, Yb^{3+}, Er^{3+}/Tm^{3+} tri-doped β-$NaYF_4$ UCNPs have been developed. In particular, the water absorption coefficient at 808 nm is less than 1/20 of that at 976 nm[26,27]. The absorption cross-section of Nd^{3+} at 805 nm (4.9×10^{-20} cm^2) is larger than that of Yb^{3+} at 976 nm (1.8×10^{-20} cm^2)[30]. The efficient energy transfer from Nd^{3+} to Yb^{3+} ions can make Nd^{3+} sensitized UCNPs with high quantum yield.[31] Various kinds of Nd^{3+}, Yb^{3+}, Er^{3+}(Tm^{3+}) tri-doped UCNPs with designs of multiple shells have been extensively reported.[32–37]

A few of reports showed that 808 nm excitation produced brighter upconversion emission in Yb/Er(Tm)@Yb@Nd/Yb UCNPs, compared with 980 nm excitation[34,36], while identical or lower brightness was observed in other reports[26,30,32,33]. These comparisons were the results measured by ensemble spectroscopy, and less quantitative due to the controls in the number of nanoparticles and excitation power densities. The upconversion process from single nanoparticles remains unclear.

In this work, we systematically investigated the upconversion behaviours and electron population mechanisms at a single nanoparticle level using 976 nm and 808 nm excitations with a large dynamic range of power densities, from 60 W/cm^2 to 7.6 MW/cm^2. We followed the design and controlled synthesis of eight batches of Yb^{3+}, Nd^{3+}, Er^{3+}-doped β-$NaYF_4$ UCNPs with the core and three-layer shells. We observed that the brightness of single UCNPs displayed a helix shape power-dependent evolution process under 976 nm and 808 nm excitation. This explains the contradictory reports around the upconversion intensities by comparing 808 nm excitation and 980 nm excitation. We then conducted the synthesis and comprehensive high-dimensional spectroscopy analysis of single nanoparticles, including the power-dependent lifetimes, emission spectra, and the wavelength-dependent power-intensity double-log slopes. We revealed the underpinning mechanism for the helix phenomenon as that at high power density 808 nm excitation Nd^{3+} ions can switch their role from being a sensitizer in the $Nd^{3+}\rightarrow Yb^{3+}\rightarrow Er^{3+}$ energy transfer network to acting as an emitter by directly producing upconversion emissions. By assessing all the eight different batches of nanoparticles, we further prove that the helix phenomenon universally exists.

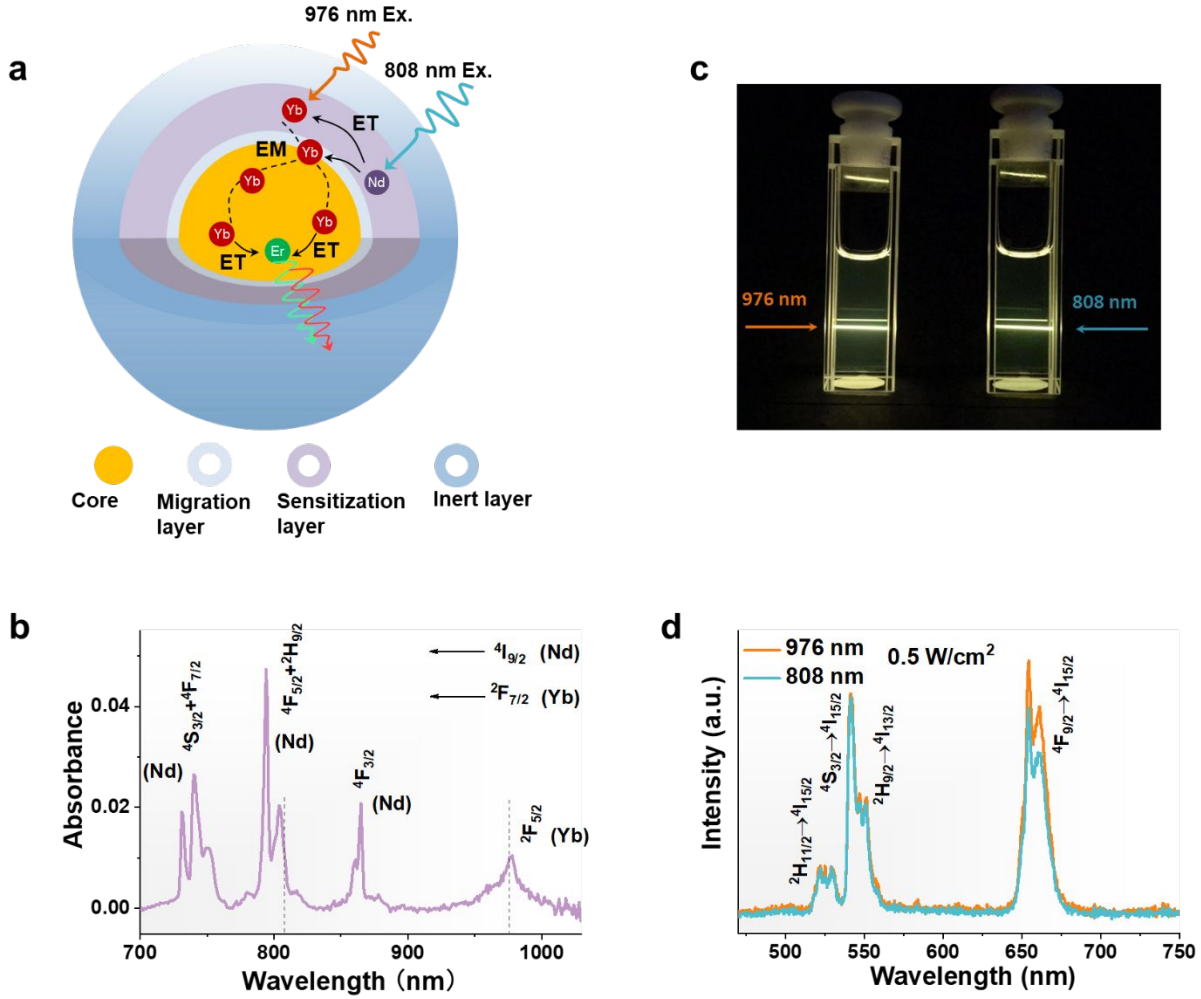

Figure1. Structure design and optical property of the colloidal UCNPs in cyclohexane. (a) Schematic illustration of the core multi-shell nanostructure and energy transfer processes under the excitations at 976 nm and 808 nm. **(b)** Absorption spectrum of $NaYF_4$:30%Yb:2%Er@$NaYF_4$:5%Yb@ $NaYF_4$:15%Yb:20%Nd@$NaYF_4$ nanoparticles (denoted by sample I). The dashed lines guide the easy reading of absorbance at 808 nm and 976 nm. **(c)** Luminescence photograph of the colloidal sample I in cyclohexane (20 mg/mL) excited by 976 and 808 nm lasers (0.5 mW/cm^2). **(d)** Upconversion emission spectra of the colloidal sample I upon 976 nm (orange) and 808 nm (blue) excitation.

Figure 1a shows design structure of UCNPs, consisting of a β-$NaYF_4$: Yb, Er core (~30 nm in diameter), migration layer doped with Yb^{3+} (~2.5 nm), sensitization layer doped with Nd^{3+} and Yb^{3+} (~6 nm), and inert layer (~5 nm). The Nd^{3+} ions serve as the sensitizer to harvest 808 nm excitation energy, which results in the population of the $^4F_{5/2}$ excited state. The Yb^{3+} ion is used as the secondary sensitizer by passing on the energy from Nd^{3+} to β-$NaYF_4$: Yb, Er core or as the primary sensitizer to directly absorb 976 nm laser excitation. The energy migrated or sensitized via Yb^{3+} will eventually reach the β-$NaYF_4$: Yb, Er core for upconversion emission by the activator Er^{3+} ions embedded in the inner core. Figure 1b shows the absorption spectrum of sample I ($NaYF_4$: 30%Yb, 2%Er@ $NaYF_4$: 5%Yb@ $NaYF_4$:15%Yb, 20%Nd@$NaYF_4$, Supplementary Fig. S1), in which the absorption band centred at ~ 800 nm is attributed to Nd^{3+}: $^4I_{9/2}$ to $^4F_{5/2}$ transition and 980 nm band is from Yb^{3+}: $^2F_{7/2}$ to $^2F_{5/2}$ transition. The absorbance at the wavelength of 808 nm (used for Nd^{3+}-excitation) is almost identical to that at 976 nm (used for Yb^{3+}-excitation). The luminescence photograph and upconversion emission spectra for ensemble colloidal nanoparticles (Figure 1c and 1d, Supplementary Fig.

S2), show nearly identical intensity profiles under 808 nm and 976 nm excitation at a power density of 0.5 W/cm^2.

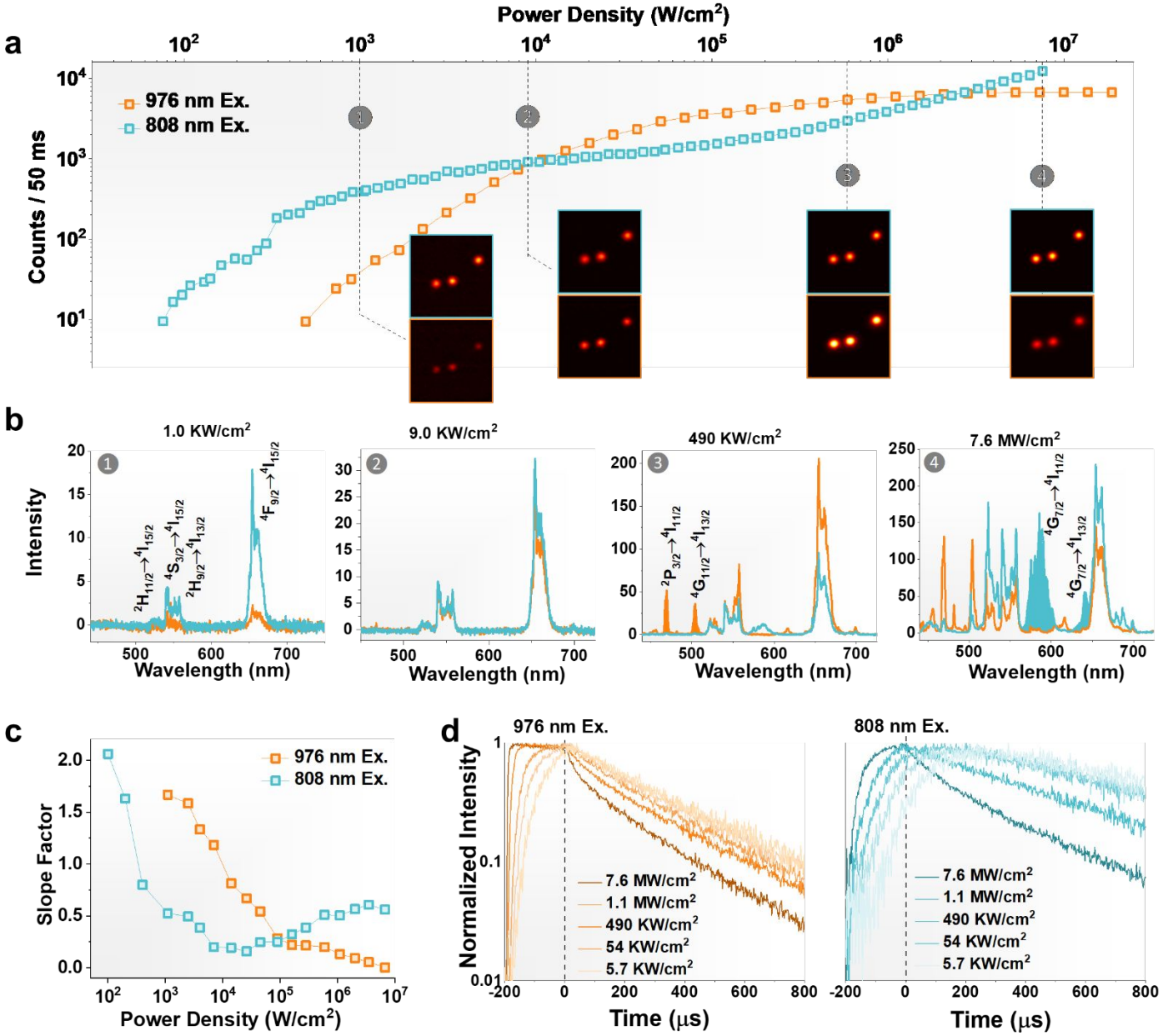

Figure 2. Single nanoparticle optical characterization of sample I. (a) Single nanoparticle intensity of sample I between 400 nm and 742 nm wavelength region as the function of power density under 976 nm and 808 nm excitation. Insets show the corresponding confocal images at four power densities (dotted grey line, 1.0 KW/cm^2, 9.0 KW/cm^2, 490 KW/cm^2, 7.6 MW/cm^2). **(b)** Single nanoparticle emission spectra under the above four power densities upon 976 nm (orange) and 808 nm (blue) excitations. **(c)** Power density-dependence of the slope factor of the intensity curves in panel (a) under 976 nm and 808 nm excitation light. **(d)** The power density-dependent single nanoparticle lifetime curves, which correlate to the emission signal from the wavelengths between 400 nm and 742 nm, under 976 nm (left) and 808 nm (right) excitation with 200 μs pulse width.

To collect the optical signals from single nanoparticles, we employ a purpose-built confocal microscopy system with 976 nm and 808 nm laser beams (Supplementary Fig. S3). Figure 2a shows the power-dependent brightness values of a single nanoparticle (sample I) at 976 nm and 808 nm excitation wavelengths. Strikingly, we observe that the initial brightness under 808 nm excitation is stronger than that under 976 nm excitation. For example, at 1 KW/cm^2, 808 nm excitation produces the brightness of 390 photon counts/50ms, which is ten times stronger compared with 976 nm excitation. When increasing the power to 9 KW/cm^2, the brightness

becomes the same. Further increasing the excitation power, brightness inversion occurs two times, which forms the double helix shape relationship. Inserts are the confocal scanning images of single nanoparticles under 808 nm and 976 nm excitation with the power densities of 1 KW/cm^2, 9 KW/cm^2, 490 KW/cm^2, and 7.6 MW/cm^2, respectively.

To understand the helix shape relationship, we measured the emission spectra at different excitation power densities (Figure 2b, Supplementary Fig. S4). Both the green ($^2H_{11/2}\rightarrow{}^4I_{15/2}$, $^4S_{3/2}\rightarrow{}^4I_{15/2}$, $^2H_{9/2}\rightarrow{}^4I_{13/2}$) and red ($^4F_{9/2}\rightarrow{}^4I_{15/2}$) emission spectra of Er^{3+} can be collected at 1 KW/cm^2 and 9 KW/cm^2. We find that the electron population pathways for Er^{3+} are different for the 808 nm and 976 nm excitations (as shown in Figure 1a), which indicate the differences in brightness when the power density increases from 1 to 9 KW/cm^2. The $Nd^{3+}\rightarrow Yb^{3+}\rightarrow Er^{3+}$ cascaded energy transfer with Yb^{3+} migration network leads to the brighter Er^{3+} emissions under 808 nm in contrast to the direct $Yb^{3+}\rightarrow Er^{3+}$ energy transfer under 980 nm excitation. The significant role in the energy transfer step of $Nd^{3+}\rightarrow Yb^{3+}$ can be evidenced by the undetectable signal from the $NaYF_4$: Yb, Er core under 808 nm excitation from 1 KW/cm^2 to 9 KW/cm^2 (Supplementary Fig. S5).

For the emission spectra within the range of 9.0 - 2500 KW/cm^2 (Figure 2b), 976 nm excitation favours the three/four-photon upconversion process from higher excited states of Er^{3+} and thereby produces stronger emission intensity in contrast to 808 nm excitation. This is evidenced by the additional emissions at ~469 nm ($^2P_{3/2}\rightarrow{}^4I_{11/2}$), ~504 nm ($^4G_{11/2}\rightarrow{}^4I_{13/2}$), and strong red emission at 654 nm ($^4F_{9/2}\rightarrow{}^4I_{15/2}$) under 976 nm excitation. Further increasing the power to 1 MW/cm^2 and more, the brightness becomes saturated, though the transition probabilities from multiple excited states are different under 976 nm excitation. However, the 808 nm excitation generates stronger intensity without saturation, in which emissions from Nd^{3+} (585 nm: $^4G_{7/2}\rightarrow{}^4I_{11/2}$, 640 nm: $^4G_{7/2}\rightarrow{}^4I_{13/2}$) appear. The emission peaks of Nd^{3+} ions are assigned through Yb^{3+}/Nd^{3+} co-doped sample shown in Supplementary Fig. S6. In this situation, Nd^{3+} ions play the roles of both the sensitizer and emission activator to facilitate an efficient upconversion process.

The slope factors (Figure 2c) calculated from the power-dependent brightness can further interpret the transition dynamics. The slope factors of 976 nm excitation decrease in the whole power density range, as a result of the increased population towards saturation at the different emissive states of Er^{3+} ions. In contrast, slope factors of 808 nm excitation experience a decrease in the low power range and an increase in the high power range. The decrease indicates the low threshold to produce detectable single particle brightness and fast saturation speed for the $Nd^{3+}\rightarrow Yb^{3+}\rightarrow Er^{3+}$ cascaded energy transfer pathway, and the increase in intensity shows the upconversion directly generated from Nd^{3+} excited states at high power range. The slope factors associated with each excited state of Er^{3+} and Nd^{3+} (Supplementary Fig.S7 and Table S1) further prove that the population of Er^{3+} excited states ($^2H_{9/2}$, $^2H_{11/2}$, $^4S_{3/2}$, $^4F_{9/2}$) through $Nd^{3+}\rightarrow Yb^{3+}\rightarrow Er^{3+}$ cascaded pathway with 808 nm excitation has the lower power threshold than the 980 excited $Yb^{3+}\rightarrow Er^{3+}$ pathway. And the Nd^{3+}: $^4G_{7/2}$ excited state population has a lower power threshold than that for the high excited states ($^4G_{11/2}$, $^2P_{3/2}$, $^2D_{5/2}$) of Er^{3+} through 3-4 photon involved transitions. These competitive energy transfer and multi-photon based upconversion processes are illustrated in the energy level diagram in Figure 3.

By measuring the lifetime profiles of single nanoparticles under the pulsed 976 nm and 808 nm excitation (pulse width of 200 μs) (Figure 2d), the transient dynamics of the electron populations further reveals the energy reservoir effect of Yb^{3+} through Nd^{3+} pumping[3]>, as the rising and decay lifetime curves response a lot of slower for 808 nm excitation compared with 976 nm excitation (Supplementary Table 2S, Supplementary Fig.S8). The high excitation power density induced shorter decay times. This is because the high excitation energy promotes the high excited states of Er^{3+} (e.g., $^2D_{5/2}$, $^2P_{3/2}$) with a shorter intrinsic lifetime to be populated and long lifetime intermediate excited states of Er^{3+} (e.g., $^4S_{3/2}$, $^2H_{9/2}$, $^4F_{9/2}$) to be depopulated [18,39,40].

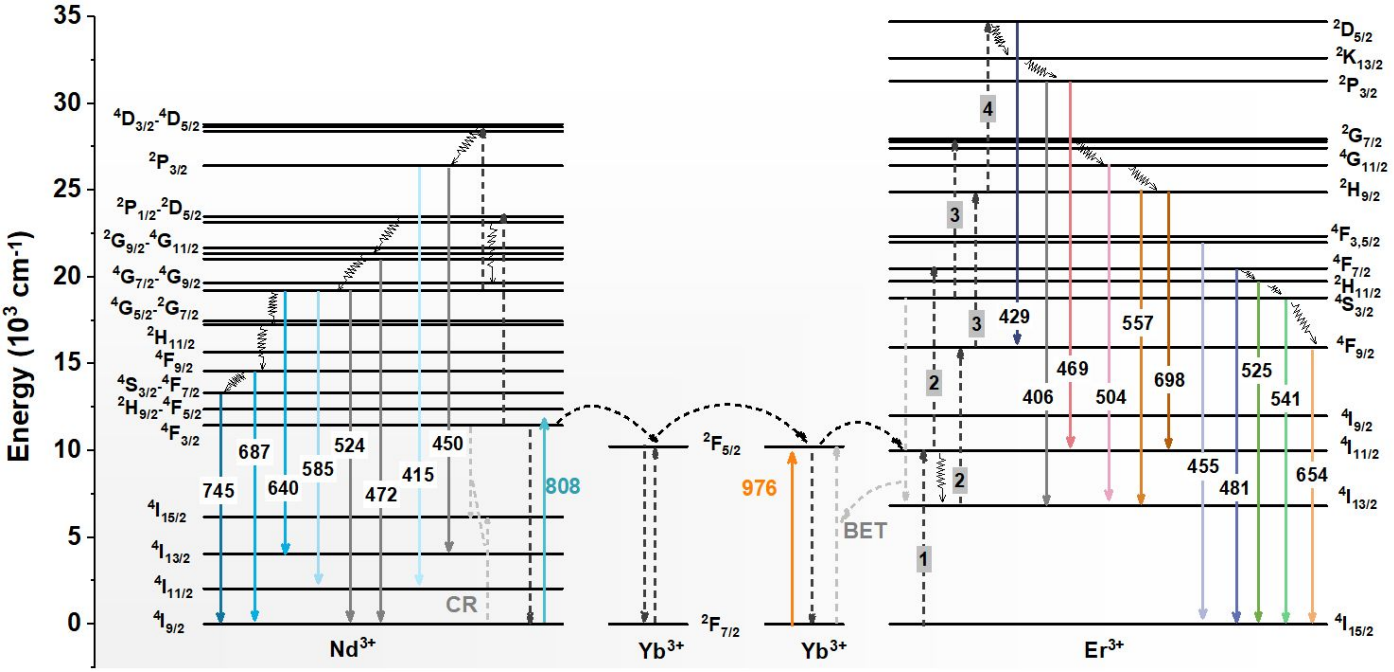

Figure 3. Energy transfer diagram of Nd^{3+}-Yb^{3+}-Er^{3+} multiphoton upconversion in four-layer core multi-shell system following excitation with a 976 nm and 808 nm laser. CR and BET represent the back energy transfer and cross-relaxation process.

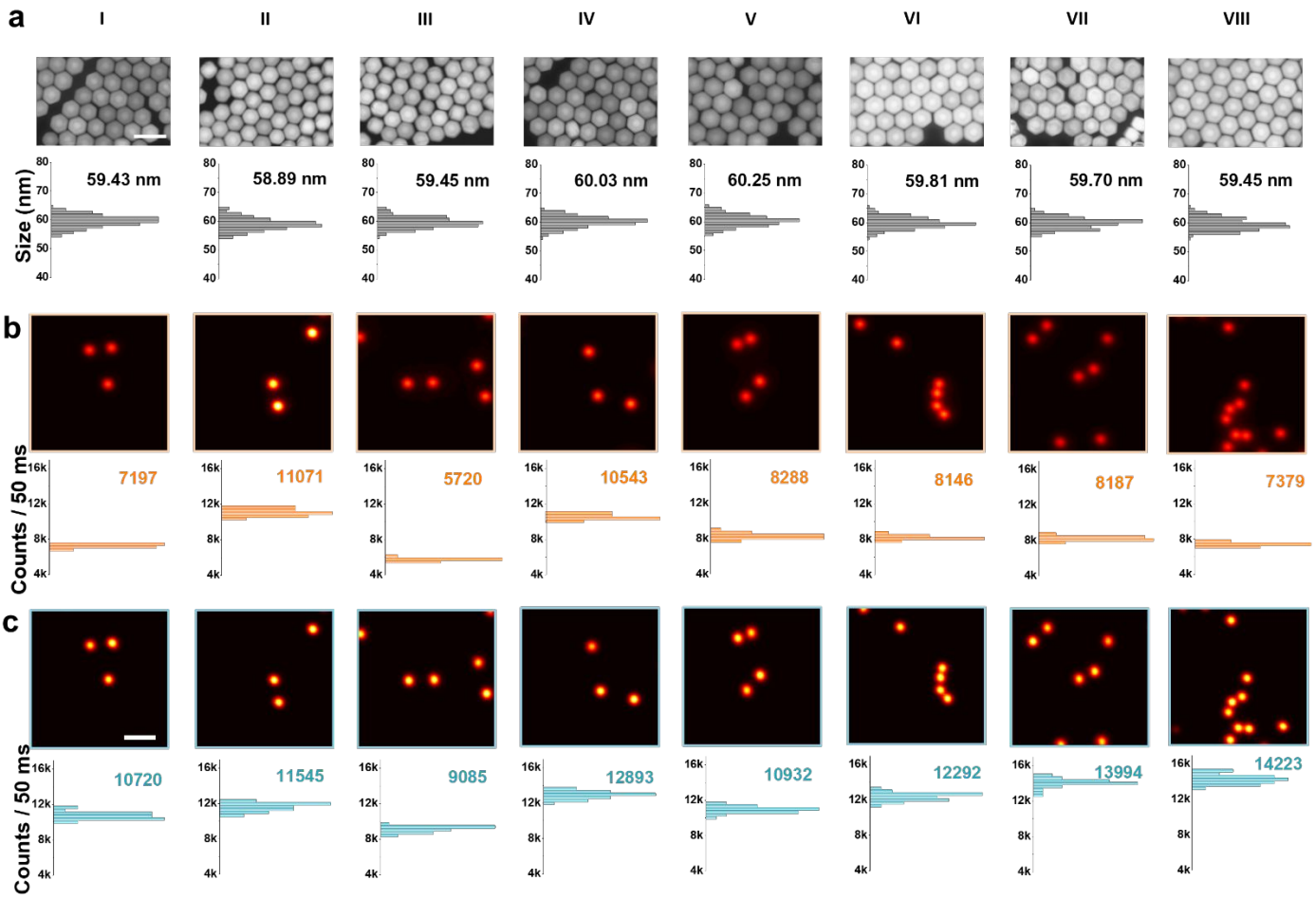

Figure 4. Uniform morphology and brightness of single core multi-shell UCNPs from the eight batches of controlled synthesis experiments. (a) HAADF-STEM characterization and size distribution histograms of approximately 200 nanoparticles for eight kinds of nanocrystals with varying doping concentrations in core and sensitization layer. The eight samples are sample I ($NaYF_4$:30%Yb:2%Er@$NaYF_4$:5%Yb@$NaYF_4$:15%Yb:20%Nd@$NaYF_4$), sample II ($NaYF_4$:30%Yb:8%Er@$NaYF_4$:5%Yb@$NaYF_4$:15%Yb:20%Nd@$NaYF_4$), sample III ($NaYF_4$:20%Yb:2%Er@$NaYF_4$:5%Yb@$NaYF_4$:15%Yb:20%Nd@$NaYF_4$), sample IV ($NaYF_4$:40%Yb:2%Er@$NaYF_4$:5%Yb@$NaYF_4$:15%Yb:20%Nd@$NaYF_4$), sample V ($NaYF_4$:30%Yb:2%Er@$NaYF_4$:5%Yb@$NaYF_4$:5%Yb:20%Nd@$NaYF_4$), sample VI ($NaYF_4$:30%Yb:2%Er@$NaYF_4$:5%Yb@$NaYF_4$:30%Yb:20%Nd@$NaYF_4$), sample VII ($NaYF_4$:30%Yb:2%Er@$NaYF_4$:5%Yb@$NaYF_4$:15%Yb:40%Nd@$NaYF_4$), sample VI ($NaYF_4$:30%Yb:2%Er@$NaYF_4$:5%Yb@$NaYF_4$:15%Yb:60%Nd@$NaYF_4$). Scale bar: 100 nm. (**b and c**) Confocal microscopic quantitative measurement of whole spectrum luminescence emission of corresponding single Nd^{3+}-Yb^{3+}-Er^{3+} UCNPs under 976 nm **(b)** and 808 nm **(c)** excitations at 7.6 MW/cm^2 and the corresponding emission intensity statistics from approximately 30 single nanoparticles. Scale bar: 2 μm.

The observed the helix shape relationship commonly exists in Nd^{3+}-Yb^{3+}-Er^{3+} tri-doped UCNPs. We synthesized eight arbitrary types of core multi-shell nanoparticles (Supplementary Table. S3). Figure 4a shows that all the controlled synthesis produces uniform core multi-shell nanostructures under scanning transmission electron microscopy (STEM). The histograms of their size distribution (grey) show that all the four-layer core multi-shell UCNPs have a similar size of ~60 nm. TEM images and size distribution statistics in Supplementary Fig. S9-14 shows the corresponding uniform core (~30 nm), core-shell (~35 nm) and core-shell-shell (~50 nm) structures. We quantified the brightness of the eight batches of single nanoparticles using confocal microscopy approach under 976 nm and 808 nm excitation at 7.6 MW/cm^2 (Figure 4b and 4c), which show the great intensity uniformity of single nanoparticles from each batch. Quantitative statistics show the peak brightness of sample I-VIII appear at 7197, 11071, 5720, 10543, 8288, 8146, 8187, 7379 counts/50ms

under 976 nm excitation and 10720, 11545, 9085,12893, 10932, 12292, 13994, 14223 counts/50ms under 808 nm excitation, respectively. Notably, 808 nm excitation consistently produces stronger brightness for all the samples compared with 976 nm excitation.

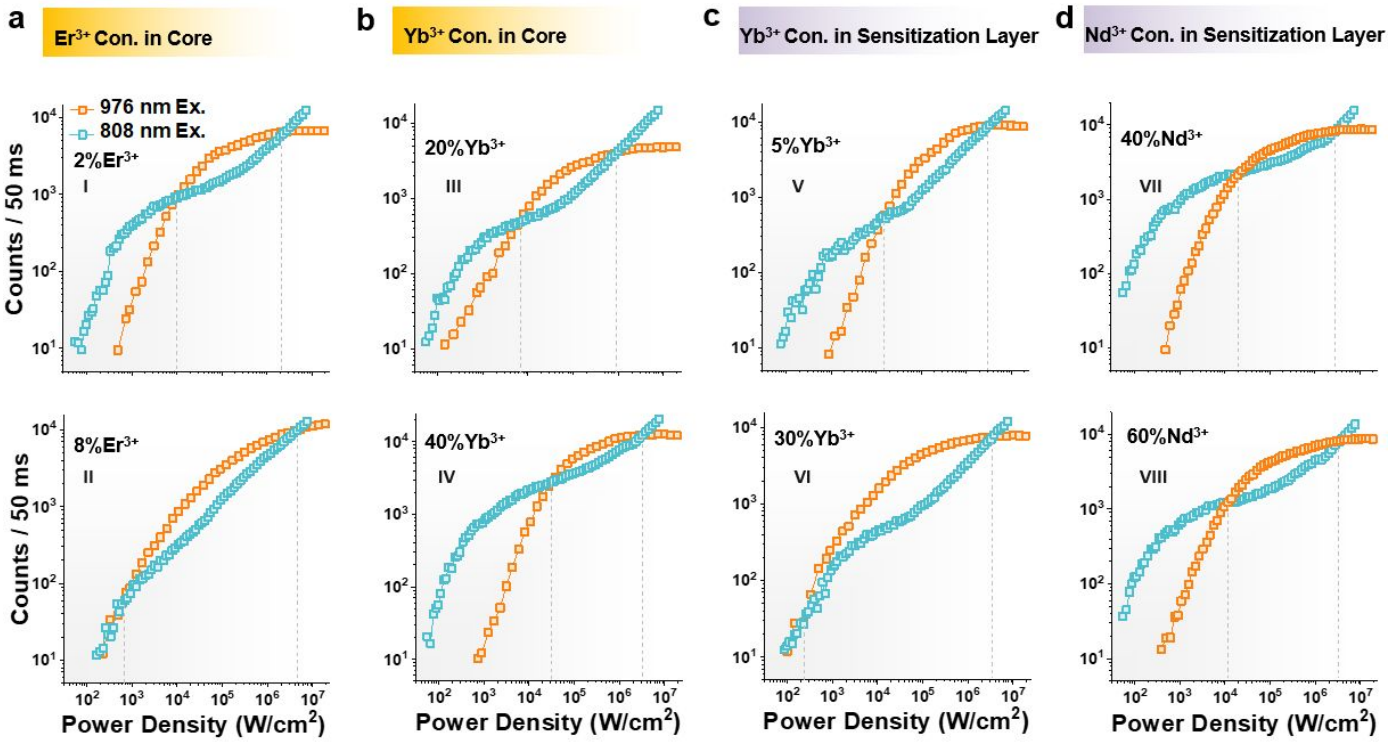

Figure 5. The power-dependent intensity curves of eight different types of single nanoparticles under 976 nm and 808 nm excitations. (a-d) The comparison of the emission intensity as the function of power density under 976 nm and 808 nm excitations for sample I and II (a), sample III and IV (b), sample V and VI (c), and sample VII and VIII (d).

Figure 5 summarizes the power-dependent evolution curves for the eight types of single Nd^{3+}-Yb^{3+}-Er^{3+} tri-doped UCNPs following the different doping concentrations and the same core multi-shell design pattern. We assigned them into four groups, according to the doping strategy, in which we varied the concentration of Er^{3+} in the core (Figure 5a) for sample I (2%Er^{3+}) and II (8%Er^{3+}), the concentration of Yb^{3+} in the core (Figure 5b) for sample III (20%Yb^{3+}) and IV(40%Yb^{3+}), the concentration of Yb^{3+} in the sensitization layer (Figure 5c) for sample V (5%Yb^{3+}) and VI (30%Yb^{3+}), and the concentration of Nd^{3+} in the sensitization layer (Figure 5d) for sample VII (40%Nd^{3+}) and VIII (60%Nd^{3+}). We observe the universal double helix shape power-brightness relationship under the 976 nm and 808 nm excitations. We show that the helix shapes (especially at the low power range) and the power density values for the first cross nodes can be tuned. The tunability for the second crossing-node at high power range is limited due to the same electron population behaviours, once the brightness being saturated at 980 nm excitation and direct upconversion emission from Nd^{3+} being generated at 808 nm excitation. The detailed upconversion emission spectra upon 976 nm and 808 nm excitation at 7.6 MW/cm^2 are shown in Supplementary Fig. S15 and Figure 2b.

The first crossing-node is tunable at the low power range by increasing the Er^{3+} concentration in the core (Figure 5a), as the emitter concentration quenching occurs. The brightness of sample II for 808 nm and 976 nm excitations became dark and overlapped, along with the small power value at the first cross node compared

with sample I. Increasing the Yb^{3+} concentration in the core (Figure 5b) can facilitate the energy transfer from Nd^{3+} to Er^{3+} under 808 nm excitation[4]>, but induce back-energy-transfer from the $^4S_{3/2}$ state of Er^{3+} to the ground state of a neighbouring Yb^{3+} ion under 976 nm excitation[42]. The sample brightness under 808 nm excitation is enhanced significantly but dropped under 976 nm excitation, and thereby the first crossing-node moves to high power density value. By increasing the Yb^{3+} concentration from 5% to 30% in the sensitization layer (Figure 5c), stronger absorption capability of 976 nm light (Supplementary Fig. S16) leads to brighter upconversion (Supplementary Fig. S17a). While an optimized Yb^{3+} concentration in the sensitization layer is necessary to avoid luminescence quenching.[43] The optimized concentration could be around 15%, as sample I (with 15%Yb^{3+} in the sensitization layer) shows the brightness superiority compared with sample V (5% Yb^{3+}) and sample VI (30% Yb^{3+}) under the low power 808 nm excitation (Supplementary Fig. S17b). By increasing the Nd^{3+} concentration in the sensitization layer (Figure 5d), strong absorption of the 808 nm light benefits the bright upconversion (Supplementary Fig. S18), but interionic cross-relaxation of Nd^{3+} ($^4F_{3/2}$, $^4I_{9/2}\rightarrow{}^4I_{15/2}$, $^4I_{15/2}$)[44] (Figure 3) will quench the overall emission brightness. This trade-off leads to the optimized concentration of Nd^{3+} in the sensitization layer around 40% under 808 nm excitation (Supplementary Fig. S17 d). Tuning the Nd^{3+} concentration in the sensitization layer doesn't affect the 976 nm excitation case. There is no obvious change in the brightness from the three samples under 976 nm excitation (Supplementary Fig. S17 c). We also confirmed this helix shape phenomenon exists in the structure with three-layer core multi-shell nanoparticles (Supplementary Fig. S19).

In summary, we conducted a systematic spectroscopic characterization of Nd^{3+}-Yb^{3+}-Er^{3+} tri-doped single UCNPs under 976 nm and 808 nm excitations and revealed the emission intensities non-linearly evolute a double helix shape relationship as the function of excitation power density at 976 nm and 808 nm. This phenomenon has been universally observed in a series of four-layer core multi-shell Nd^{3+}-Yb^{3+}-Er^{3+} doped UCNPs. The helix shape is highly dependent on the doping concentrations of lanthanides in the heterogeneous structure of active core, migration layer, sensitization layer and inert layer of shells, suggesting that the population dynamics of each excited state highly depend on the power-dependent energy transfer pathways under the excitations of 976 nm and 808 nm lasers. This study reveals the insights that can be used for improving the efficiency of single UCNPs and non-linearity behaviours of them for advanced imaging and sensing applications.

REFERENCE

(1) Zhou, B.; Shi, B.; Jin, D.; Liu, X. Controlling Upconversion Nanocrystals for Emerging Applications. *Nature Nanotechnology*. 2015, 10 (11), 924–936.

(2) Yang, D.; Hou, Z.; Cheng, Z.; Li, C.; Lin, J. Current Advances in Lanthanide Ion (Ln^{3+})-Based Upconversion Nanomaterials for Drug Delivery. *Chem. Soc. Rev.* **2015**, *44* (6), 1416–1448.

(3) Gai, S.; Li, C.; Yang, P.; Lin, J. Recent Progress in Rare Earth Micro/Nanocrystals: Soft Chemical

Synthesis, Luminescent Properties, and Biomedical Applications. *Chem. Rev.* **2014**, *114* (4), 2343–2389.

(4) Park, Y.; Lee, K.; Suh, Y.; Hyeon, T. Upconverting Nanoparticles: A Versatile Platform for Wide-Field Two-Photon Microscopy and Multi-Modal in Vivo Imaging. *Chem.Soc.Rev.* **2015**, *44* (6), 1302–1317.

(5) Zeng, X.; Chen, S.; Weitemier, A.; Han, S.; Blasiak, A.; Prasad, A.; Zheng, K.; Yi, Z.; Luo, B.; Yang, I. H.; et al. Visualization of Intra-Neuronal Motor Protein Transport through Upconversion Microscopy. *Angew. Chemie - Int. Ed.* **2019**, *58* (27), 9262–9268.

(6) Zheng, W.; Huang, P.; Tu, D.; Ma, E.; Zhu, H.; Chen, X. Lanthanide-Doped Upconversion Nano-Bioprobes: Electronic Structures, Optical Properties, and Biodetection. *Chem. Soc. Rev.* **2015**, *44* (6), 1379–1415.

(7) Chen, S.; Weitemier, A.; Zeng, X.; He, L.; Wang, X.; Tao, Y.; Huang, A.; Hashimotodani, Y.; Kano, M.; Iwasaki, H.; et al. Near-Infrared Deep Brain Stimulation via Upconversion Nanoparticle–mediated Optogenetics. *Science.* **2018**, *359* (6376), 679–684.

(8) Zheng, W.; Tu, D.; Huang, P.; Zhou, S.; Chen, Z.; Chen, X. Time-Resolved Luminescent Biosensing Based on Inorganic Lanthanide-Doped Nanoprobes. *Chem. Commun.* **2015**, *51* (20), 4129–4143.

(9) Mi, C.; Zhou, J.; Wang, F.; Lin, G.; Jin, D. Ultrasensitive Ratiometric Nanothermometer with Large Dynamic Range and Photostability. *Chem. Mater.* **2019**, *31* (22), 9480–9487.

(10) Chen, G.; Damasco, J.; Qiu, H.; Shao, W.; Ohulchanskyy, T. Y.; Valiev, R. R.; Wu, X.; Han, G.; Wang, Y.; Yang, C.; et al. Energy-Cascaded Upconversion in an Organic Dye-Sensitized Core/Shell Fluoride Nanocrystal. *Nano Lett.* **2015**, *15* (11), 7400–7407.

(11) Zheng, K.; Loh, K. Y.; Wang, Y.; Chen, Q.; Fan, J.; Jung, T.; Nam, S. H.; Suh, Y. D.; Liu, X. Recent Advances in Upconversion Nanocrystals: Expanding the Kaleidoscopic Toolbox for Emerging Applications. *Nano Today* **2019**, 100797.

(12) Brites, C. D. S.; Xie, X.; Debasu, M. L.; Qin, X.; Chen, R.; Huang, W.; Rocha, J.; Liu, X.; Carlos, L. D. Instantaneous Ballistic Velocity of Suspended Brownian Nanocrystals Measured by Upconversion Nanothermometry. *Nat. Nanotechnol.* **2016**, *11* (10), 851–856.

(13) Huang, P.; Zheng, W.; Tu, D.; Shang, X.; Zhang, M.; Li, R.; Xu, J.; Liu, Y.; Chen, X. Unraveling the Electronic Structures of Neodymium in $LiLuF_4$ Nanocrystals for Ratiometric Temperature Sensing. *Adv. Sci.* **2019**, *6* (10), 1802282.

(14) Deng, R.; Qin, F.; Chen, R.; Huang, W.; Hong, M.; Liu, X. Temporal Full-Colour Tuning through Non-Steady-State Upconversion. *Nat. Nanotechnol.* **2015**, *10* (3), 237–242.

(15) Lu, Y.; Zhao, J.; Zhang, R.; Liu, Y.; Liu, D.; Goldys, E. M.; Yang, X.; Xi, P.; Sunna, A.; Lu, J.; et al. Tunable Lifetime Multiplexing Using Luminescent Nanocrystals. *Nat. Photonics* **2014**, *8* (1), 32–36.

(16) Zhao, J.; Jin, D.; Schartner, E. P.; Lu, Y.; Liu, Y.; Zvyagin, A. V.; Zhang, L.; Dawes, J. M.; Xi, P.; Piper, J. A.; et al. Single-Nanocrystal Sensitivity Achieved by Enhanced Upconversion Luminescence. *Nat. Nanotechnol.* **2013**, *8* (10), 729–734.

(17) Liu, Q.; Zhang, Y.; Peng, C. S.; Yang, T.; Joubert, L. M.; Chu, S. Single Upconversion Nanoparticle Imaging at Sub-10 W cm^{-2} Irradiance. *Nat. Photonics* **2018**, *12* (9), 548–553.

(18) Gargas, D. J.; Chan, E. M.; Ostrowski, A. D.; Aloni, S.; Altoe, M. V. P.; Barnard, E. S.; Sanii, B.; Urban, J. J.; Milliron, D. J.; Cohen, B. E.; et al. Engineering Bright Sub-10-nm Upconverting Nanocrystals for Single-Molecule Imaging. *Nat. Nanotechnol.* **2014**, *9* (4), 300–305.

(19) Chen, C.; Wang, F.; Wen, S.; Su, Q. P.; Wu, M. C. L.; Liu, Y.; Wang, B.; Li, D.; Shan, X.; Kianinia, M.; et al. Multi-Photon near-Infrared Emission Saturation Nanoscopy Using Upconversion Nanoparticles. *Nat. Commun.* **2018**, *9* (1), 1–6.

(20) Zhan, Q.; Liu, H.; Wang, B.; Wu, Q.; Pu, R.; Zhou, C.; Huang, B.; Peng, X.; Ågren, H.; He, S. Achieving High-Efficiency Emission Depletion Nanoscopy by Employing Cross Relaxation in Upconversion Nanoparticles. *Nat. Commun.* **2017**, *8* (1), 1–11.

(21) Liu, Y.; Lu, Y.; Yang, X.; Zheng, X.; Wen, S.; Wang, F.; Vidal, X.; Zhao, J.; Liu, D.; Zhou, Z.; et al. Nanoparticles for Super-Resolution Nanoscopy. *Nat. Publ. Gr.* **2017**, *543* (7644), 229–233.

(22) Jin, D.; Xi, P.; Wang, B.; Zhang, L.; Enderlein, J.; Van Oijen, A. M. Nanoparticles for Super-Resolution Microscopy and Single-Molecule Tracking. *Nature Methods*. 2018, 15(6), 415–423.

(23) Mickert, M. J.; Soukka, T.; Lahtinen, S.; Tallgren, T.; Gorris, H. H. Large-Scale Purification of Photon-Upconversion Nanoparticles by Gel Electrophoresis for Analogue and Digital Bioassays. *Anal. Chem.* **2019**, *91* (2), 1241–1246.

(24) He, H.; Liu, B.; Wen, S.; Liao, J.; Lin, G.; Zhou, J.; Jin, D. Quantitative Lateral Flow Strip Sensor Using Highly Doped Upconversion Nanoparticles. *Anal. Chem.* **2018**, *90* (21), 12356–12360.

(25) Farka, Z.; Mickert, M. J.; Hlaváček, A.; Skládal, P.; Gorris, H. H. Single Molecule Upconversion-Linked Immunosorbent Assay with Extended Dynamic Range for the Sensitive Detection of Diagnostic Biomarkers. *Anal. Chem.* **2017**, *89* (21), 11825–11830.

(26) Wang, Y.; Liu, G.; Sun, L.; Xiao, J.; Zhou, J.; Yan, C.; Al, W. E. T. Nd^{3+}-Sensitized Upconversion Nanophosphors: Efficient in Vivo Bioimaging Probes with Minimized Heating Effect. *ACS Nano* **2013**, *7* (8), 7200–7206.

(27) Weissleder, R. A Clearer Vision for in Vivo Imaging. *Nat. Biotechnol.* **2001**, *19* (4), 316–317.

(28) Zhan, Q.; Qian, J.; Liang, H.; Somesfalean, G.; Wang, D.; He, S.; Zhang, Z.; Andersson-Engels, S. Using 915 nm Laser Excited $Tm^{3+}/Er^{3+}/Ho^{3+}$-Doped $NaYbF_4$ Upconversion Nanoparticles for in Vitro and Deeper in Vivo Bioimaging without Overheating Irradiation. *ACS Nano* **2011**, *5* (5), 3744–3757.

(29) Chen, Q.; Xie, X.; Huang, B.; Liang, L.; Han, S.; Yi, Z.; Wang, Y.; Li, Y.; Fan, D.; Huang, L.; et al. Confining Excitation Energy in Er^{3+}-Sensitized Upconversion Nanocrystals through Tm^{3+}-Mediated Transient Energy Trapping. *Angew. Chemie - Int. Ed.* **2017**, *56* (26), 7605–7609.

(30) Wiesholler, L. M.; Frenzel, F.; Grauel, B.; Würth, C.; Resch-Genger, U.; Hirsch, T. Yb,Nd,Er-Doped Upconversion Nanoparticles: 980 nm versus 808 nm Excitation. *Nanoscale* **2019**, *11* (28), 13440–13449.

(31) Chen, G.; Damasco, J.; Qiu, H.; Shao, W.; Ohulchanskyy, T. Y.; Prasad, P. N. Energy-Cascaded Upconversion in an Organic Dye-Sensitized Core/Shell Fluoride Nanocrystal. *Nano Lett.* **2015**, *15* (11), 7400–7407.

(32) Xie, X.; Gao, N.; Deng, R.; Sun, Q.; Xu, Q.; Liu, X. Mechanistic Investigation of Photon Upconversion in Nd^{3+}sensitized Core−shell Nanoparticles. *J. Am. Chem. Soc* **2013**, *135* (34), 12608–12611.

(33) Shen, J.; Chen, G.; Vu, A. M.; Fan, W.; Bilsel, O. S.; Chang, C. C.; Han, G. Engineering the Upconversion Nanoparticle Excitation Wavelength: Cascade Sensitization of Tri-Doped Upconversion Colloidal Nanoparticles at 800 nm. *Advanced Optical Materials*. 2013, 1(9), 644–650.

(34) Zhong, Y.; Tian, G.; Gu, Z.; Yang, Y.; Gu, L.; Zhao, Y.; Ma, Y. Elimination of Photon Quenching by a Transition Layer to Fabricate a Quenching-Shield Sandwich Structure for 800 nm Excited Upconversion Luminescence of Nd^{3+}-Sensitized Nanoparticles. *Adv. Mater* **2014**, *26* (18), 2831–2837.

(35) Liu, B.; Li, C.; Yang, P.; Hou, Z.; Lin, J. 808-nm-Light-excited Lanthanide-doped Nanoparticles: Rational Design, Luminescence Control and Theranostic Applications. *Adv. Mater.* **2017**, *29* (18), 1605434.

(36) Wang, S.; Shen, B.; Wei, H. L.; Liu, Z.; Chen, Z.; Zhang, Y.; Su, Y.; Zhang, J. Z.; Wang, H.; Su, Q. Comparative Investigation of the Optical Spectroscopic and Thermal Effect in Nd^{3+}-Doped Nanoparticles. *Nanoscale* **2019**, *11* (21), 10220–10228.

(37) Xie, X.; Li, Z.; Zhang, Y.; Guo, S.; Pendharkar, A. I.; Lu, M.; Huang, L.; Huang, W.; Han, G. Emerging≈ 800 Nm Excited Lanthanide-Doped Upconversion Nanoparticles. *Small* **2017**, *13* (6), 1602843.

(38) Zuo, J.; Sun, D.; Tu, L.; Wu, Y.; Cao, Y.; Xue, B.; Zhang, Y.; Chang, Y.; Liu, X.; Kong, X.; et al. Precisely Tailoring Upconversion Dynamics via Energy Migration in Core-Shell Nanostructures.

Angew. Chemie **2018**, *130* (12), 3108–3112.

(39) Alyatkin, S.; Asharchuk, I.; Khaydukov, K.; Nechaev, A.; Lebedev, O.; Vainer, Y.; Semchishen, V.; Khaydukov, E. The Influence of Energy Migration on Luminescence Kinetics Parameters in Upconversion Nanoparticles. *Nanotechnology* **2017**, *28* (3), 035401.

(40) Sun, T.; Li, Y.; Ho, W. L.; Zhu, Q.; Chen, X.; Jin, L.; Zhu, H.; Huang, B.; Lin, J.; Little, B. E.; et al. Integrating Temporal and Spatial Control of Electronic Transitions for Bright Multiphoton Upconversion. *Nat. Commun.* **2019**, *10* (1), 1–7.

(41) Zhong, Y.; Rostami, I.; Wang, Z.; Dai, H.; Hu, Z. Energy Migration Engineering of Bright Rare-Earth Upconversion Nanoparticles for Excitation by Light-Emitting Diodes. *Adv. Mater.* **2015**, *27* (41), 6418–6422.

(42) Wang, J.; Deng, R.; Macdonald, M. A.; Chen, B.; Yuan, J.; Wang, F.; Chi, D.; Andy Hor, T. S.; Zhang, P.; Liu, G.; et al. Enhancing Multiphoton Upconversion through Energy Clustering at Sublattice Level. *Nat. Mater.* **2014**, *13* (2), 157–162.

(43) Song, N.; Zhou, B.; Yan, L.; Huang, J.; Zhang, Q. Understanding the Role of Yb^{3+} in the Nd/Yb Coupled 808-Nm-Responsive Upconversion. *Frontiers in Chemistry*. 2019, p 673.

(44) Borrero-González, L. J.; Nunes, L. A. O. Near-Infrared Quantum Cutting through a Three-Step Energy Transfer Process in Nd^{3+}-Yb^{3+} Co-Doped Fluoroindogallate Glasses. *J. Phys. Condens. Matter* **2012**, *24* (38), 385501.

Acknowledgments: This project is primarily supported by ARC Discovery Early Career Researcher Award Scheme (J.Z., DE180100669), Science and Technology Innovation Commission of Shenzhen (KQTD20170810110913065), Australia-China Joint Research Centre for Point-of-Care Testing (ACSRF65827, SQ2017YFGH001190), China Scholarship Council Scholarships (Jiayan Liao: No. 201508530231). Thanks to the support of Mark Lockrey for the STEM characterization.

Table of Contents (TOC)

The Yb^{3+}, Nd^{3+}, Er^{3+}-doped nanoparticles with the core-multi-shell structure are synthesized by hot-injection method. The brightness evolution displays a pair of double helix shapes as the function of power densities of 976 nm and 808 nm excitations. This non-linear responsive properties from upconversion nanoparticles could be controlled through doping design, which is useful for imaging and sensing.

Keyword: upconversion, power-dependent properties, single particle

Jiayan Liao[1], Dayong Jin[1,2], Chaohao Chen[1], Yiming Li[3], Jiajia Zhou[1,*]

Helix shape power-dependent properties of single upconversion nanoparticles